



City Research Online

City St George's, University of London

Citation: Reyes-Aldasoro, C. C., Wilson, I., Prise, V. E., Barber, P. R., Ameer-Beg, M., Vojnovic, B., Cunningham, V. J. & Tozer, G. M. (2008). Estimation of apparent tumor vascular permeability from multiphoton fluorescence microscopic images of P22 rat sarcomas in vivo. *Microcirculation*, 15(1), pp. 65-79. doi: 10.1080/10739680701436350

This is the accepted version of the paper.

This version of the publication may differ from the final published version. To cite this item please consult the publisher's version.

Permanent repository link: <https://openaccess.city.ac.uk/id/eprint/5510/>

Link to published version: <https://doi.org/10.1080/10739680701436350>

Copyright and Reuse: Copyright and Moral Rights remain with the author(s) and/or copyright holders. Copies of full items can be used for personal research or study, educational, or not-for-profit purposes without prior permission or charge, unless otherwise indicated, provided that the authors, title and full bibliographic details are credited, a hyperlink and/or URL is given for the original metadata page and the content is not changed in any way. For full details of reuse please refer to [City Research Online policy](#).

Title:

Estimation of Apparent Tumour Vascular Permeability from Multiphoton Fluorescence
Microscopic Images of P22 Rat Sarcomas *in vivo*.

Authors:

Constantino Carlos Reyes-Aldasoro ^a; Ian Wilson ^b; Vivien E. Prise ^b; Paul R. Barber ^b;
Simon M. Ameer-Beg ^c; Borivoj Vojnovic ^b; Vincent J. Cunningham ^d; Gillian M. Tozer ^a

Address:

^a Cancer Research UK Tumour Microcirculation Group, Academic Unit of Surgical
Oncology, The University of Sheffield, Sheffield, UK

^b Mount Vernon Hospital, Gray Cancer Institute, Northwood, Middlesex, UK

^c The Richard Dimbleby Department of Cancer Research, Division of Cancer Studies,
King's College, London, London, UK

^d GlaxoSmithKline, Clinical Imaging Centre, Imperial College, London, UK

*Corresponding author.

E-mail address: c.reyes@sheffield.ac.uk

Telephone: 00 44 (0) 114 271 2850

Fax: 00 44 (0) 114 271 3791

Running Title:

Measurement of Tumour Vascular Permeability

Acknowledgements:

This work has been supported by Cancer Research UK.

ABSTRACT

Objective: To develop an image processing-based method to quantify the rate of extravasation of fluorescent contrast agents from tumour microvessels, and to investigate the effect of the tumour vascular disrupting agent, combretastatin A-4-P (CA-4-P), on apparent tumour vascular permeability to 40 kDa fluorescein isothiocyanate (FITC) labelled dextran.

Methods: Extravasation of FITC-dextran was imaged in three dimensions over time within P22 sarcomas growing in dorsal skin flap 'window chambers' in BDIX rats using multiphoton fluorescence microscopy. Image processing techniques were used to segment the data into intra- and extra-vascular regions or classes. Quantitative estimates of the tissue influx (vascular leakage) rate constant, K_i , were obtained from the time courses of the fluorescence intensities in the two classes. Apparent permeability, P , was calculated, assuming $K_i = PS/V$, where S is vascular surface area in tumour volume V .

Results: Combining image processing and kinetic analysis algorithms with multi-photon fluorescence microscopy enabled quantification of the rate of tumour vascular leakage, averaged over a large number of vessels. Treatment with CA-4-P caused a significant increase in K_i from 1.13 ± 0.33 to 2.59 ± 0.20 ($\text{s}^{-1} \times 10^{-4}$; mean \pm SEM), equivalent to an increase in P from 12.76 ± 3.36 to 30.94 ± 2.64 ($\text{cm s}^{-1} \times 10^{-7}$).

Conclusions: A methodology was developed that provided evidence for a CA-4-P-induced increase in tumour macromolecular vascular permeability, likely to be central to its anti-cancer activity.

Keywords: Vascular permeability, multiphoton fluorescence microscopy, combretastatin, segmentation, tumour vascular disrupting agents.

INTRODUCTION

Vascular permeability of blood vessels in tumours is of great interest for the treatment of cancer for three main reasons. First, the vascular wall represents a major barrier to the entry of high molecular weight anti-cancer agents into tumour tissue [1]; second, it controls the tumour microenvironment thus affecting tumour progression [2] and third, changes in its barrier function may provide an early indicator of vascular damage following treatment with anti-angiogenic or vascular disrupting drugs [3]. Despite the importance of tumour vascular permeability [4], little attention has been paid to its quantitative measurement. In some cases, permeability is simply observed by using a marker, for example Evans blue, an albumin-binding dye, and determining if the marker is present or absent in a specific tissue region [5-7]. Although this is useful in normal tissues, where any significant extravasation is suggestive of vascular damage or in determining breakdown of the blood-brain barrier following tumour growth, it is not appropriate for determining the effects of treatment in tumours, where even unperturbed blood vessels are highly permeable. In this case, a fully quantitative method is required.

The first aim of the present work was to develop methodology to quantify the rate of extravasation of an intravenously-administered macromolecular fluorescent marker from microvessels over a large tumour volume, using multiphoton fluorescence microscopy. The advent of multiphoton fluorescence microscopy has allowed 3-D optical imaging *in vivo* of tissue at greater depth than confocal microscopy, with very precise geometric localisation of the fluorophore and high spatial resolution [8]. This minimizes problems such as scattered light from out-of-focus regions, associated with conventional fluorescence microscopy [9]. To take full quantitative advantage of this technique we have applied image processing and kinetic analysis techniques to obtain estimates of K_i , the vascular leakage or tissue influx rate constant into tumour tissue of intravenously administered fluorescent dextran. In addition, the capillary vascular surface area, S , and

the vascular volume, V_{vess} within a given tumour volume, V , were measured to enable calculation of an apparent vascular permeability, P .

The second aim of the study was to investigate the effect of the tumour vascular disrupting agent, combretastatin A-4-phosphate (CA-4-P) on tumour vascular permeability. CA-4-P is a tubulin binding agent, which has been shown to depolymerise the tubulin cytoskeleton of vascular endothelial cells *in vitro*, within minutes of drug exposure, and to selectively shut down tumour blood flow *in vivo* [10-13]. These vascular disrupting effects led to its entry into clinical trials as an anti-cancer agent in 1998, where it is currently being tested in combination with conventional chemo- and radiotherapy. It has been hypothesised from *in vitro* data [14] that an increase in vascular permeability to macromolecules is an early effect of CA-4-P *in vivo*, indicative of vascular damage. Indeed, we have previously reported a *relative* increase in tumour extravasation of a macromolecular radiotracer following CA-4-P treatment [12]. However, we were unable to obtain absolute rates of extravasation in that study and the spatial resolution was poor. Here we report application of the above multiphoton fluorescence microscopy technique to the quantitative estimation of the apparent vascular permeability of tumour micro-vessels following CA-4-P treatment.

MATERIALS AND METHODS

Overview

The P22 rat sarcoma was grown in transparent dorsal skin flap 'window' chambers to provide optically accessible tumour preparations for multiphoton fluorescence microscopy. 3-D images of the leakage of intravenously administered 40 kDa FITC-dextran into the tumour extra-vascular space were obtained over time in CA-4-P and saline-treated rats. Image-processing techniques were applied to segment the images

into intra- and extra-vascular tissue classes. A kinetic analysis was applied to the time-courses of fluorescence in these classes to obtain estimates of parameters relating to vascular permeability.

Animals and Tumours

The experiments were performed in male BDIX rats aged 6-8 weeks, weighing approximately 200 g. All animals were bred in house. All animal procedures were carried out in accordance with the UK Animals (Scientific Procedures) Act 1986 and with approval of the Ethical Review Committee of the Gray Cancer Institute. Single small fragments (approximately $0.5 \times 0.5 \times 0.5 \text{ mm}^3$) of early generation P22 rat sarcomas grown subcutaneously in donor rats were placed in contact with connective tissue held in transparent window chambers surgically implanted into the dorsal skin flap of recipient rats. Details of this technique have been described previously [12]. Immediately following surgery, animals were given an intra-peritoneal (i.p.) injection of 2 ml of dextrose saline and allowed to recover from anaesthesia on a warm pad. The animals were subsequently kept in a warm room, 32 – 34 °C, until the day of the experiment. The tumours were allowed to establish over a period of 10-14 days after surgery to a diameter of 2 to 4 mm.

Preparation of Fluorophores

FITC-dextran (40 kDa, 0.013Mol FITC/Mol dextran) (Sigma, Poole, UK) was made up in phosphate buffered saline (PBS) and washed through a 30 kDa spin filter at 4000 rpm in a Sorvall RC-5B refrigerated fixed angle superspeed centrifuge (Dupont, Stevenage, UK). Two washes of 4 hrs and one of 16 hrs were applied to remove any free FITC or low molecular weight contaminants. The high molecular weight component was re-suspended in PBS after each wash and used for investigation of fluorophore stability or multiphoton fluorescence microscopy, as described below.

Fluorophore stability

Non-tumour-bearing rats were surgically anaesthetized using a mixture of fentanyl-citrate (0.32 mg/kg) and fluanisone (10 mg/kg; Hypnorm; Janssen Animal Health) and midazolam (5 mg/kg; Hypnovel; Roche, Welwyn Garden City, United Kingdom) and kept warm with a thermostatically controlled heating blanket. One tail vein and one tail artery were cannulated and 0.1 ml of heparin (100 IU) followed by 40 mg/kg (20 mg/ml) FITC-dextran were injected intravenously. Blood samples (0.5 ml) were taken via the arterial cannula at various time-points up to 2 hours following fluorophore injection. Blood cells were removed by spinning at 3000 rpm for 5 minutes. 0.2 ml of plasma from each sample was diluted to 1 ml in PBS and centrifuged through a 30 KDa spin filter (Millipore, Watford, UK), separating the plasma into two fractions, one containing high molecular weight (> 30 KDa) and one containing low molecular weight (< 30 KDa) fluorescent components. Both high and low molecular weight components were then measured for fluorescence intensity using a spectrometer (Perkin Elmer, Beaconsfield, UK). Samples were excited at 450 nm and fluorescent emission collected between 470 nm and 650 nm.

Multiphoton Intravital Microscopy

Rats were surgically anaesthetized and kept warm as above. A tail vein was cannulated to permit intra-venous administration of the FITC-dextran. 0.5 ml FITC-dextran, at a concentration of 20mg/ml, was injected via the venous cannula as a bolus over 2-3 seconds, immediately prior to image acquisition. Image acquisition was instigated as soon as the microscope could be focused on the fluorescence, approximately one minute after injection.

Microscopy was performed with a multiphoton microscope system developed in-house, although commercial systems with similar specifications are now available. The in-house system was based on a modified Bio-Rad MRC 1024MP workstation, comprising a solid state pumped (10 W Millennia X, Nd:YVO₄, Spectra Physics), self mode locked Ti:Sapphire (Tsunami, Spectra Physics) laser system, a focal scan head, confocal detectors and an inverted microscope (Nikon TE200). Enhanced detection of the scattered component of the emitted (fluorescence) photons is enabled by the use of three, non-descanned detectors, situated in the re-projected stationary plane. Due to geometrical constraints of the animal model, a long working distance objective was used; all images were captured with a 10x Nikon Plan Fluor objective (16 mm WD, 0.3 NA).

Data collection

CA-4-P (30 mg/kg) or an equivalent volume of saline was administered i.p. immediately prior to injection of fluorophore. Multiphoton fluorescent images were collected every 4 minutes, at a working excitation wavelength of 890 nm. Emission wavelength was 530 nm to 540 nm.

The 3-D data consisted of 512 x 512 x 11 voxels each of volume 2.6 x 2.6 x 4.5 μm^3 . Fluorescence intensity, captured by the acquisition process, was assumed to be directly proportional to the number of molecules of the fluorescent marker. 15 time-frames were acquired over 60 minutes. Figure 1 shows the acquisition process graphically and illustrates the marker leaking from the intra-vascular tissue over time. A total of 15 animals were imaged, of which 9 were treated with CA-4-P, and 6 were controls.

Image Pre-processing

Pre-processing of the data was required to address two important problems: presence of noise, and tissue movement with time. All the image and statistical processing was performed in MATLAB (The Mathworks, USA ©).

In order to reduce the noise in the 3-D volumes, a standard Oct Tree [15] averaging was performed, where the intensities of a number of neighbouring elements, 8 voxels in our case, are averaged. This procedure was carried out once, so that the final analysis was performed on 256 x 256 x 6 voxels.

In order to correct for tissue movement, a tissue registration process was employed. The window chamber glass limited the movement of the tissue in the third dimension, reducing the degrees of freedom. Therefore, in most cases, the registration (i.e. correction of the image motion) was performed with a rigid body registration. In these cases, the whole image in each time-frame was moved and aligned to match the image in the previous time-frame. In a few cases, the tissue movement was not uniform, with parts of the image moving in different directions over time. In these cases, the data was partitioned into 15 x 15 regions of 32 x 32 x 6 voxels with 50% overlap and a local rigid body registration was performed for each of them individually. For both scenarios, the displacement of the data was analysed and corrected through cross correlation [16]. Cross correlation is a measurement of similarity or 'matching' between two signals; if two signals are identical, their relative similarity at the origin will be 1; if they are different, relative similarity will be less than 1, and if one of them has moved, the relative similarity will present a maximum value displaced from the origin according to the movement of the signal. The accuracy of the registration was assessed visually, which is a generally accepted method [17].

Segmentation

Following pre-processing corrections, the images corresponding to the first time point were segmented into intra-vascular and extra-vascular classes using a double threshold masking technique as described below. The masks, defining the class to which each voxel from the corresponding intensity image belonged were applied to all subsequent intensity images of the same tumour in order to obtain intensity versus time within both intra-vascular and extra-vascular classes.

Voxels below a lower threshold were classified as extra-vascular, and those above a higher threshold were classified as intravascular. Lower and higher thresholds were first set to enclose 50% and 95% of the voxels respectively. Optimisation of the threshold levels for each data set was then obtained by manual adjustment based on a visual inspection of the segmented classes. The remaining voxels, between these two levels, were then classified as follows.

The intra-vascular class was smoothed by a convolution (i.e. a weighted average of each voxel and its neighbours sometimes called a Local Energy Function) with a [3 x 3 x 3] Gaussian kernel [18]. This gives rise to a boundary region, defined as voxels adjacent to the intra-vascular class, hence allowing the surface area (in cm^2) of the vessels (S) to be calculated. The volume (in cm^3) of the vessels (V_{vess}) was calculated by the sum of the number of voxels of the intra-vascular class. Finally, isolated elements were eroded and reassigned to the class of their neighbours [19]. Remaining voxels were classified as uncertain.

Validation of the segmentation algorithm

Images from the first time-frame from two tumours were segmented manually using methodology described previously [20], without any knowledge of classification obtained by the segmentation algorithms described above. Briefly, manual segmentation of the

images involved placing a series of points by eye along the length of individual vessels, at the estimated mid-point between the vascular walls, and recording the (x,y,z) coordinates. Wherever a vessel branching point was found, it was marked and a new trace started. A 'vessel' was defined as the length traced between two branching points. The average number of points in a vessel was approximately 10. The first tumour set required 1415 points in 124 vessels and the second set required 3292 points in 385 vessels. The (x,y,z) coordinates of these points were then used to determine whether the current segmentation technique allocated them correctly. A vessel was considered as identified correctly if more than 50% of the manually described points for that vessel were found within either the intra-vascular or boundary classes.

Kinetic analysis of extravasation

Segmentation allowed the extraction of fluorescence intensity-time curves for the intra-vascular class (capillary input function) and the corresponding curve for the extra-vascular class (tissue response function). In order to simplify the kinetic analysis of this extravasation data, we employed a graphical representation originally described by Patlak *et al.* [21], which is widely used in quantitative imaging studies [22], such as those employing magnetic resonance imaging (MRI) ([23-25]) and positron emission tomography (PET) [26-29]. This method involves a transformation of the data such that the ratio of extra-vascular intensity to intra-vascular intensity is plotted against a modified time axis, which effectively transforms the data into that which would have been observed had the capillary input function been constant throughout the experiment. This transformation greatly simplifies the analysis. When there is a net irreversible accumulation of fluorescence in the tissue over the time course of the experiment, it follows that the plot becomes linear after sufficient equilibration time. Also, the terminal slope of this line is equal to the rate constant describing the net irreversible transport of

the fluorescence from the capillary to the tissue (K_i) [21]. See also Padhani and Choyke [22] for a text-book description of the Patlak approach.

The modified time axis in this plot is calculated as follows [21]: for each real time point, t , of the experiment, the modified time, T , is given by the integrated concentration of marker in blood up to time t divided by the actual concentration of the marker at time t .

Therefore, for our data, the Patlak plot is given by $y = \frac{C_t(t)}{C_{vess}(t)}$ against $T = \frac{\int C_{vess}(t)dt}{C_{vess}(t)}$,

where $C_t(t)$ is fluorescence intensity in the extra-vascular class and $C_{vess}(t)$ is fluorescence intensity in the intra-vascular class at time t . In order to fit the transformed data and obtain an estimate of the terminal slope, we used an equation describing an exponential approach to a straight line $y = (\alpha + \beta T)(1 - e^{-\gamma T})$, with variables α , β and γ , where the slope of this straight line, β , is the estimate of K_i . Data were fitted using non-linear least mean squares. The average time required for image processing and kinetic analysis algorithms, from the intensity data to K_i for each tumour, was of the order of minutes.

Estimation of Apparent Permeability

Since the resolution of multiphoton fluorescence microscopy allowed the measurements of the input function to be performed directly in the microvessels, estimates of an apparent vascular permeability, P , were obtained from the relationship $K_i = PS/V$ (in sec^{-1}) [30-32], where S is vascular surface area for exchange in a volume V of exchanging tumour tissue, obtained from the image analysis described above.

Statistics

A Student's t-test was used to test the significance of the difference in means between the control and CA-4-P-treated groups for the different permeability parameters. The analysis was performed using MATLAB's Statistics Toolbox.

RESULTS

Fluorophore stability

5 minutes after intravenous administration of 40 kDa FITC-dextran, the high molecular weight component ($> 30\text{kDa}$) of plasma fluorescence accounted for 99.8% of the total fluorescence measured in rat plasma. This percentage remained constant throughout the time-course of the experiment (2 hours). Total plasma fluorescence decreased from approximately 4×10^4 to 2.5×10^4 fluorescence intensity units, over the same time-scale, presumably due to tissue uptake and metabolism. Maintenance of the high molecular weight component of fluorescence over this time-scale provided evidence for *in vivo* stability of the FITC-dextran used in the imaging studies.

Image Pre-processing

The tissue movement with time of one of the data sets is presented in two different ways in figure 2; first as a 'time cut' (figure 2 (a)) and then as one dimensional (1-D) lines (figure 2 (b)). In figure 2 (a), the top image is the time cut, formed by selecting a line of intensity values from the same position in each of the intensity images and placing the lines from images belonging to adjacent time points next to each other. Intensity images from three separate time points are shown in the lower panels in figure 2 (a). It can be seen that the intensities for the chosen line shift upwards and later downwards with time, indicating tissue movement. Another characteristic of the time cut shown is the decreasing contrast in intensities with time, indicating leakage of FITC-dextran from the intra-vascular to extra-vascular space. Figure 2 (b) shows two 1-D signals corresponding to one line of voxels from the time cut at two different time points. The tissue movement is revealed by a clear shift to the left of the intensity profile with time.

Figure 3 illustrates the results for cross correlation, used in image registration to correct for tissue movement with time. The relative similarity of the two 1-D signals shown in figure 2 (b) is presented in figure 3 (a). The peak of the cross correlation, indicating 95% relative similarity, is shifted towards the right of the centre, indicating movement i.e. the line in the image at the second time point is most similar to the selected line in the first image when it has moved to the right by approximately 20 μm . In figure 3 (b) the cross correlation of two 2-D signals is presented as a 3-D mesh and again it can be seen there is a shift in the rows, while there is no apparent movement in the columns. The arrow indicates the movement of the tissue, so that its registration was performed by a shift in the inverse direction.

Figures 3 (c, d) show two different registration maps, the first corresponds to a case where rigid registration would correct the movement of the tissue and the second corresponds to a movement that requires a non-rigid registration to compensate for the movement of the tissue. The maps were obtained by partitioning the data into 15 x 15 regions of 32 x 32 x 6 voxels as described in Materials and Methods. Each arrow denotes the correction required for each region of the partition. Finally figure 3 (e) shows a time cut image of the registered data derived from the raw data shown in figure 2 (a). The registration process has turned the curved lines corresponding to the bright intra-vascular tissue into straight lines.

Validation of the segmentation algorithm

The semi-automated segmentation algorithm described above, applied to all 15 tumour data sets, gave overall classification of voxels as 8.8% intra-vascular, 67.8% extra-vascular, 18.1% boundary, and 5.3% uncertain.

Two tumour sets were used for validation, as described in Materials and Methods. In the first tumour, 12.9% of the vessels were designated incorrectly as extra-vascular and

87.1% were designated correctly as intra-vascular. For the second set, the results were 7.0% and 93.0% respectively. Figure 4 shows the semi-automated segmentation, as a 3-D rendering of the class masks for two tumours (a, b), the maximum intensity projections for both sets (c, d) and the results of the comparison between semi-automated segmentation and manual vessel identification (e, f). In e) and f), the vessels labelled in white and black indicate correct and incorrect classification by the semi-automated algorithm respectively. The vessels that were classified incorrectly were mainly due to vessels with very low intensity, as indicated by the arrows in Figure 4 for example.

To evaluate the effect of omitting the incorrectly classified vessels in the analysis, we measured the average fluorescence intensities of the hand-segmented vessels for both tumours, firstly using only the correctly classified vessels and secondly using all the vessels. In the first tumour, the average intra-vascular fluorescence intensity was 51.6 for correctly classified vessels only and 48.3 for all vessels. In the second tumour, the corresponding values were 41.9 and 40.6. The corresponding extra-vascular levels were 19 for the first tumour and 8.7 for the second. The difference in intensities calculated by the two segmentation methods accounted for a variation of 6.4% and 3.2% in the C_t/C_{vess} ratio for the two tumours respectively, and therefore had minimal impact on calculations of the apparent vascular permeability.

Estimation of Apparent Tumour Vascular Permeability

The time-courses of intra- and extra-vascular fluorescence intensity are illustrated in figure 5 (a) with one control and one CA-4-P treated tumour. The intra-vascular intensity (C_{vess}) decreased rapidly in the first 20 minutes of the experiment, as expected due to whole body clearance of FITC-dextran. There was a significant difference in the rate of extravasation of the marker between controls and CA-4-P-treated tumours. As shown in Table 1, there was a significant difference between the two groups in the ratio C_t/C_{vess} at the final time point. The rate of extravasation was also quantified in a Patlak analysis, as

described in Materials and Methods. Figure 5 (b) shows representative Patlak plots for the same control and CA-4-P-treated tumours as in figure 5 (a). As described previously, in these plots, the C_t/C_{vess} ratio is plotted against a modified time axis T , equivalent to a tissue response to a constant concentration of the fluorescence marker in the vasculature. The linear increase in the ratio is indicative of a net irreversible accumulation of the marker in the extra-vascular regions of the tumour. The terminal slope of the line, K_i , was significantly greater in the CA-4-P-treated tumours than in the controls, as shown in Table 1 and figure 5 (c).

The vessel volume and surface area per unit tumour volume (V_{vess}/V) and (S/V) respectively were also calculated and values are given in Table 1. A mean value of 0.083 for V_{vess}/V in control tumours or 0.091 for the CA-4-P-treated tumours at the start of the experiment (Table 1) are reasonable values for vascular volume for the well-vascularised P22 tumour and is similar to the value reported by Yuan [9] for a different tumour model. The value for S/V enables expression of the rate of extravasation in terms of the capillary surface area, to give an apparent permeability P , where, P equals $K_i \times V/S$. P was significantly greater in the CA-4-P-treated tumours than in the control tumours, as shown in Table 1 and figure 5 (d). The impact of the segmentation thresholds was assessed by varying the optimum thresholds for each set and re-calculating P . No significant difference was detected for variations of ± 2 in the grey level intensity (approximately 10% of the optimal value) in the levels of both thresholds (results not shown).

DISCUSSION

The present work builds on the inherent properties of multiphoton fluorescence microscopy for measuring the precise spatial localization of fluorescence at depth in

tissue. Application of image processing and kinetic analysis techniques to multiphoton fluorescence images of the uptake of a fluorescent marker into tumour tissue allowed estimation of the apparent tumour vascular permeability and its modification following vascular-targeted treatment. 40 kDa FITC-dextran was found to have prolonged stability in rat plasma. In contrast, we have found that administration of FITC-labelled albumin to rats results in a significant proportion of fluorescence in a low molecular weight fraction of plasma, within 20 minutes of injection, suggestive of significant instability of this molecule *in vivo* (unpublished data).

There are several advantages of the methodology used here. The high spatial resolution of optical techniques allows direct segmentation of the intra-vascular input function from the tissue response function. This avoids the confounding effect that blood flow has on the interpretation of K_i , when the input function is either assumed or measured in great vessels, as used in other lower resolution imaging modalities such as magnetic resonance imaging and positron emission tomography. Had the input function been measured in arterial blood then it would have been necessary to take into account the effects on K_i of both blood flow rate and the transport rate across the capillary walls, as modelled for example in the Renkin-Crone equation [30,31]. The high spatial resolution of optical techniques combined with the use of multiphoton fluorescence for obtaining 3-D images also allows supplementary measures of capillary surface area and volume to be taken into account when interpreting K_i in terms of apparent permeability, P . Because of the acquisition of 3-D images, this does not involve any assumptions regarding vessel diameter in the depth dimension. Furthermore, the semi-automated method used here allows full use to be made of the 3-D data set instead of manual selection of a very small sub-set of blood vessels within the imaged volume. User intervention is required only for setting the intensity thresholds, and no vessel selection or repositioning is required. The segmentation and analysis with the proposed

methodology takes a matter of minutes, whilst manual tracing of blood vessels within a tumour, as described in [20] takes many hours. Furthermore, it was possible to minimize movement effects by application of image registration techniques to images obtained at consecutive time points.

Two important observations regarding the segmentation technique used in the current study arise at this point. First, even if parts of vessels were incorrectly classified as extra-vascular tissue, those regions that were classified as intra-vascular were almost certainly correct such that the numbers of false positives were very low. Clearly, if the upper threshold that defines the intra-vascular tissue were lowered, more points would belong to this class, but at the same time the number of false positives would also rise, lowering the specificity of the method. Second, the geometry of the vasculature was only of secondary interest for this work; such that disjointed or broken vessels could be tolerated for estimation of K_i , as long as the average intensity of each class was determined accurately. In other words, the sensitivity of the method to distinguish vessels with low intensity is less crucial than the correctness of classes it detects.

Graphical representation of leakage data, as described by Patlak *et al.* [21], is a useful analysis tool as it avoids the use of complex pharmacokinetic modelling, in the case of net irreversibly accumulation of a marker in the extra-vascular space. In addition, in our case, it allows easy visual assessment of the effect of CA-4P, which is not immediately apparent from inspection of the original time-activity curves, where the capillary input function is not constant. The early part of the transformed curves, such as the ones shown in Figure 5b), cannot be accurately defined because of the time required to focus the microscope. However, this is not critical because it is the terminal slope of the 'Patlak plot' from which estimates of K_i are obtained.

Our estimation of apparent permeability, P , derives from $K_i = PS/V$ [32]. We have denoted P as an *apparent* permeability because its relationship to the true physico-

chemical permeability for the chosen marker requires several qualifications, which are often ignored in the literature. Strictly, the concentration of the intra-vascular fluorescent marker should be expressed relative to plasma rather than whole blood. This correction to the estimate of P would require knowledge of the haematocrit in individual micro-vessels. We have also assumed that the K_i is limited by the uni-directional transport of the fluorophore from capillary across the vascular wall and that there is no significant reversible exchange occurring during the time-course of the experiment. We aimed to minimize these effects by the use of a high molecular weight marker but we cannot discount their existence. In the presence of reversible exchange of the fluorophore across the capillary wall, the K_i would represent a lower bound estimate for PS/V . Finally, we refer to P as an apparent permeability because an unknown proportion of leakage occurs via convection currents. This is discussed in more detail below, with respect to the CA-4-P-induced increase in K_i .

In [33] Gerlowski reported vascular permeability (P) measurements of $5.72 \pm 3.92 \times 10^{-7}$ cm/s for FITC-dextran 150 (150 kDa) in tumours grown in rabbit ear chambers. In [2] Monsky reported $3.2 \pm 13 \times 10^{-7}$ cm/s (mammary fat pad) and $1.3 \pm 0.5 \times 10^{-7}$ cm/s (cranial window) for tetramethylrhodamine-labeled BSA in ZR75-1 tumours growing in different microenvironments in female severe combined immunodeficient (SCID) mice. In [9] Yuan reported $6.06 \pm 4.30 \times 10^{-7}$ cm/s for Texas Red-BSA (67 kDa) in human adenocarcinoma LS174T in SCID mice. Our value for untreated tumours was $12.76 \pm 3.36 \times 10^{-7}$ cm/s. Therefore, given the different animals, markers, molecular weights, imaging modalities and tumour lines used in the studies, our estimates of the apparent vascular permeability are of the same order as these published data. All these estimates were obtained using conventional fluorescence microscopy and are subject to the qualifications described above.

Both K_i and P were higher in the CA-4-P-treated group compared with controls. The effect of CA-4-P on K_i clearly demonstrates that the leakage rate of FITC-dextran from blood to the extra-vascular tumour space is increased after CA-4-P treatment, which implies a generalized protein leak into the tumour tissue, as previously proposed [12]. Clearly, differences in charge, size and shape of dextran compared with plasma proteins such as albumin means that the absolute P for these various macromolecules differ. However, an increase in P for dextran is highly suggestive of an increase in P for plasma proteins of similar molecular weight. The calculations of P from K_i required additional calculations of S and V from the segmented images, thus potentially introducing further uncertainties in the estimates of P . However, the p-value obtained when P was compared for the CA-4-P treated and control groups was low enough to reject the hypothesis that the two groups belonged to a single distribution.

The CA-4-P-induced increase in apparent permeability P strongly implies that CA-4-P disrupts the barrier function of tumour blood vessels. It should be pointed out that, as for several previous studies using the window chamber model, high tumour pressure imposed by the chamber glass could affect the absolute values of P obtained. Similarly, systemic cardiovascular effects of dextrans could affect the absolute values [34]. However, in terms of the effect of CA-4-P on P , both the control and treated groups were exposed to similar conditions, such that the statistical discrimination that was found between the two groups is robust. In addition, we cannot dismiss the possibility that there was an increase in fluid convection across the vascular wall following CA-4-P treatment, which could contribute to the observed increase in P . This may occur as a result of an increase in tumour perfusion pressure subsequent to a CA-4-P-induced increase in mean arterial blood pressure, as reported previously in rats [35]. Finally, a limitation of the method is that the values of permeability correspond to an average of all vessels within the data, thus ignoring regional differences in permeability. This could be

analysed separately, but the partitioning of the data would increase the uncertainty of the measurements of surface area and volume, as a lower number of elements would be used for the calculations.

In summary, the multiphoton fluorescence imaging method described allows accurate estimation of the tissue influx (vascular leakage) rate constant, K_i , further allowing estimation of the apparent tumour vascular permeability, P , for an intravenously administered high molecular weight marker, with minimal user intervention and fewer assumptions than for other imaging methods with lower spatial resolution. In addition, results showed a significant increase in K_i and P following treatment with CA-4-P, which is consistent with our *in vitro* data and may act as a trigger for tumour blood flow reduction.

ACKNOWLEDGEMENTS

We would like to thank the Biological Services staff at the Gray Cancer Institute for care of the animals and Cancer Research UK for funding this work.

REFERENCES

1. Jain RK: Delivery of novel therapeutic agents into tumours: physiological barriers and strategies. *JNCI* 1989;81:570-576.
2. Monsky WL, Mouta Carreira C, Tsuzuki Y, Gohongi T, Fukumura D, Jain RK: Role of host microenvironment in angiogenesis and microvascular functions in human breast cancer xenografts: mammary fat pad versus cranial tumors. *Clinical Cancer Research* 2002;8:1008-1013.
3. Tozer GM, Kanthou C, Baguley BC: Disrupting tumour blood vessels. *Nat Rev Cancer* 2005;5:423-435.
4. McDonald DM, Baluk P: Significance of Blood Vessel Leakiness in Cancer. *Cancer Research* 2002;62:5381-5385.
5. Baird LC, Canoll P, Bruce J: Effect of infiltrating tumor cells on the blood-brain barrier in a neonatal rat glioma model. In *Society for Neuro-Oncology Eighth Annual Meeting*. Keystone, Colorado, 2003.
6. Nakano S, Matsukado K, Black KL: Increase brain tumor microvessel permeability after intracarotid bradykinin infusion is mediated by nitric oxide. *Cancer Research* 1996;56:4027-4031.

7. Inoue N, Venema RC, Sayegh HS, Ohara Y, Murphy TJ, Harrison DG: Molecular regulation of the bovine endothelial nitric oxide synthase by transforming growth factor-beta 1. *Arterioscler Thromb Vasc Biol* 1995;15:1255-1261.
8. Masters BR, So PTC: Antecedents of Two-Photon Excitation Laser Scanning Microscopy, *Microscopy Research and Technique*. *Microscopy Research and Technique* 2004;63:3-11.
9. Yuan F, Leunig M, Berk DA, Jain RK: Microvascular permeability of albumin, vascular surface area, and vascular volume measured in human adenocarcinoma LS174T using dorsal chamber in SCID mice. *Microvasc Res* 1993;45:269-289.
10. Dark GD, Hill SA, Prise VE, Tozer GM, Pettit GR, Chaplin DJ: Combretastatin A-4, an agent that displays potent and selective toxicity toward tumor vasculature. *Cancer Res.* 1997;57:1829-1834.
11. Grosios K, Holwell SE, McGown AT, Pettit GR, Bibby MC: In vivo and in vitro evaluation of combretastatin A-4 and its sodium phosphate prodrug. *Br. J. Cancer* 1999;81:1318-1327.
12. Tozer GM, Prise VE, Wilson J, Cemazar M, Shan S, Dewhurst MW, Barber PR, Vojnovic B, Chaplin DJ: Mechanisms associated with tumor vascular shut-down induced by combretastatin A-4 phosphate: intravital microscopy and measurement of vascular permeability. *Cancer Res* 2001;61:6413-6422.
13. Tozer GM, Prise VE, Wilson J, Locke RJ, Vojnovic B, Stratford MRL, Dennis MF, Chaplin DJ: Combretastatin A-4 phosphate as a tumor vascular-targeting agent: early effects in tumors and normal tissues. *Cancer Res.* 1999;59:1626-1634.
14. Kanthou C, Tozer GM: The tumor vascular targeting agent combretastatin A-4-phosphate induces reorganization of the actin cytoskeleton and early membrane blebbing in human endothelial cells. *Blood* 2002;99:2060-2069.
15. Gaede V, Günther O: Multidimensional access methods. *ACM Computing Surveys* 1998;30:170-231.
16. de Castro E, Morandi C: Registration of translated and rotated images using finite Fourier transforms. *IEEE Transactions on Pattern Analysis and Machine Intelligence* 1987;5:700-703.
17. Hill DLG, Batchelor PG, Holden M, Hawkes DJ: Medical Image Registration [invited topical review]. *Physics in Medicine and Biology* 2001;46:R1-R45.
18. Randen T, Husøy JH: Filtering for Texture Classification: A Comparative Study. *IEEE Trans. on Patt. Anal. and Machine Intel.* 1999;21:291-310.
19. Schroeter P, Bigun J: Hierarchical Image Segmentation by Multi-dimensional Clustering and Orientation-Adaptive Boundary Refinement. *Pattern Recognition* 1995;28:695-709.
20. Barber PR, Vojnovic B, Ameer-Beg SM, Hodgkiss RJ, Tozer GM, Wilson J: Semi-automated software for the three-dimensional delineation of complex vascular networks. *J Microsc* 2003;211:54-62.
21. Patlak CS, Blasberg RG, Fenstermacher JD: Graphical evaluation of blood-to-brain transfer constants from multiple-time uptake data. *J Cereb Blood Flow Metab* 1983;3:1-7.
22. Padhani AR, Choyke PL: *New Techniques in Oncologic Imaging*. Boca Raton FL, CRC Press, 2006.
23. Daldrup H, Shames DM, Wendland M, Okuhata Y, Link TM, Rosenau W, Lu Y, Brasch RC: Correlation of dynamic contrast-enhanced MR imaging with histologic tumor grade: comparison of macromolecular and small-molecular contrast media. *AJR Am J Roentgenol* 1998;171:941-949.

24. Daldrup HE, Shames DM, Hussein W, Wendland MF, Okuhata Y, Brasch RC: Quantification of the extraction fraction for gadopentetate across breast cancer capillaries. *Magn Reson Med* 1998;40:537-543.
25. Roberts HC, Roberts TP, Ley S, Dillon WP, Brasch RC: Quantitative estimation of microvascular permeability in human brain tumors: correlation of dynamic Gd-DTPA-enhanced MR imaging with histopathologic grading. *Acad Radiol* 2002;9 Suppl 1:S151-155.
26. Romer W, Hanauske AR, Ziegler S, Thodtmann R, Weber W, Fuchs C, Enne W, Herz M, Nerl C, Garbrecht M, Schwaiger M: Positron emission tomography in non-Hodgkin's lymphoma: assessment of chemotherapy with fluorodeoxyglucose. *Blood* 1998;91:4464-4471.
27. Smith IC, Welch AE, Hutcheon AW, Miller ID, Payne S, Chilcott F, Waikar S, Whitaker T, Ah-See AK, Eremin O, Heys SD, Gilbert FJ, Sharp PF: Positron emission tomography using [(18)F]-fluorodeoxy-D-glucose to predict the pathologic response of breast cancer to primary chemotherapy. *J Clin Oncol* 2000;18:1676-1688.
28. Lodge MA, Lucas JD, Marsden PK, Cronin BF, O'Doherty MJ, Smith MA: A PET study of 18FDG uptake in soft tissue masses. *Eur J Nucl Med* 1999;26:22-30.
29. Vesselle H, Schmidt RA, Pugsley JM, Li M, Kohlmyer SG, Vallires E, Wood DE: Lung cancer proliferation correlates with [F-18]fluorodeoxyglucose uptake by positron emission tomography. *Clin Cancer Res* 2000;6:3837-3844.
30. Renkin EM: Transport of potassium-42 from blood to tissue in isolated mammalian skeletal muscles. *Am. J. Physiol.* 1959;197:1205-1210.
31. Michel CC, Curry FE: Microvascular permeability. *Physiol Rev* 1999;79:703-761.
32. Bickel U: How to Measure Drug Transport across the Blood-Brain Barrier. *NeuroRx* 2005;2:15-26.
33. Gerlowski LE, Jain R, K.: Microvascular permeability of normal and neoplastic tissues. *Microvascular Research* 1986;31:288-305.
34. Briseid G, Briseid K: Inhibition by low molecular weight dextran of the blood pressure fall and the lowering of plasminogen proactivator induced by clinical dextran in the rat. *Acta Pharmacol Toxicol (Copenh)* 1983;52:143-149.
35. Prise VE, Honess DJ, Stratford MRL, Wilson J, Tozer GM: The vascular response of tumor and normal tissues in the rat to the vascular targeting agent, combretastatin A-4-phosphate, at clinically relevant doses. *Int J Oncol* 2002;21:717-726.

TABLE 1

Estimates of vascular parameters in P22 tumours grown in dorsal skin flap window chambers with/without treatment with combretastatin A-4-P (CA-4-P). (C_t/C_{vess}) is extra-vascular versus intra-vascular fluorescence intensity ratio for the last time sample ($t = 58.5$ min); K_i is the tissue influx (vascular leakage) rate constant; V_{vess}/V is the vascular volume per unit volume of tissue; S/V is the vascular surface area per unit volume of tissue; P is the apparent tumour vascular permeability calculated from $K_i = PS/V$. Mean values, standard deviation (SD), standard error of the mean (SEM) and p-values for a Student's t-test between treated and untreated groups are also presented. Notice that while there is no statistical difference in the geometrical parameters (S/V , V_{vess}/V), the three indicators of permeability (C_t/C_{vess} , K_i , P) show a difference ($p < 0.05$) between treated cases and controls.

Table 1

Animal Number	Group	C_i/C_{vess}	$K_i * 10^4$ [1/s]	V_{vess}/V	S/V [1/cm]	$P * 10^7$ [cm/s]
1	CA-4-P	0.968	3.695	0.107	84.1	43.914
2	CA-4-P	0.795	2.061	0.067	49.9	41.258
3	CA-4-P	0.691	2.252	0.097	86.0	26.202
4	CA-4-P	0.700	3.095	0.096	107.8	28.711
5	CA-4-P	0.808	2.062	0.093	76.7	26.874
6	CA-4-P	0.797	2.456	0.091	92.8	26.471
7	CA-4-P	0.732	2.350	0.075	91.8	25.607
8	CA-4-P	0.659	3.224	0.118	85.3	37.796
9	CA-4-P	0.708	2.096	0.077	96.9	21.638
Mean		0.762	2.588	0.091	85.7	30.941
SD		0.093	0.599	0.016	16.1	7.911
SEM		0.03	0.20	0.005	5.4	2.64
10	Control	0.579	1.164	0.054	54.6	21.323
11	Control	0.460	0.492	0.082	108.9	4.516
12	Control	0.608	2.154	0.121	93.9	22.938
13	Control	0.563	2.039	0.117	134.8	15.123
14	Control	0.388	0.639	0.070	80.6	7.930
15	Control	0.661	0.278	0.056	58.9	4.721
Mean		0.543	1.128	0.083	88.6	12.758
SD		0.101	0.806	0.030	30.6	8.227
SEM		0.04	0.33	0.01	12.5	3.36
p-value		0.0008	0.0014	0.514	0.810	0.0009

FIGURES

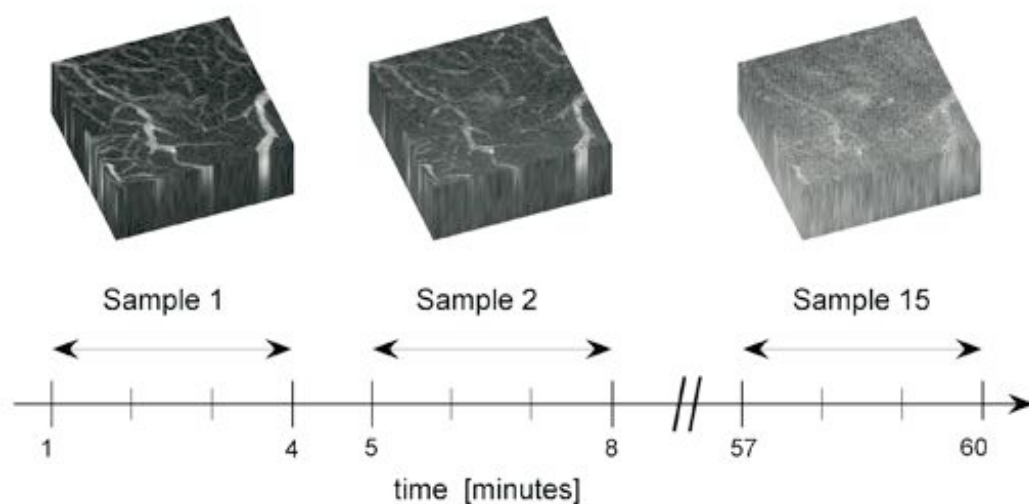


Figure 1. Time course of the acquisition of one 3-D volume ($512 \times 512 \times 11$ voxels corresponding to $1331.2 \times 1331.2 \times 50 \mu\text{m}^3$) of multiphoton images for one BDIX rat treated with CA-4-P. Intra-vascular tissue is bright at the first time point allowing its ready discrimination from surrounding tissue. Notice the reduced contrast in the tumour with time, as contrast agent leaks into the extra-vascular tissue. Time $t = 1$ was used to represent the start of image acquisition. The mid-point of each 3 minute imaging window was used to represent the acquired time for each image in all subsequent plots.

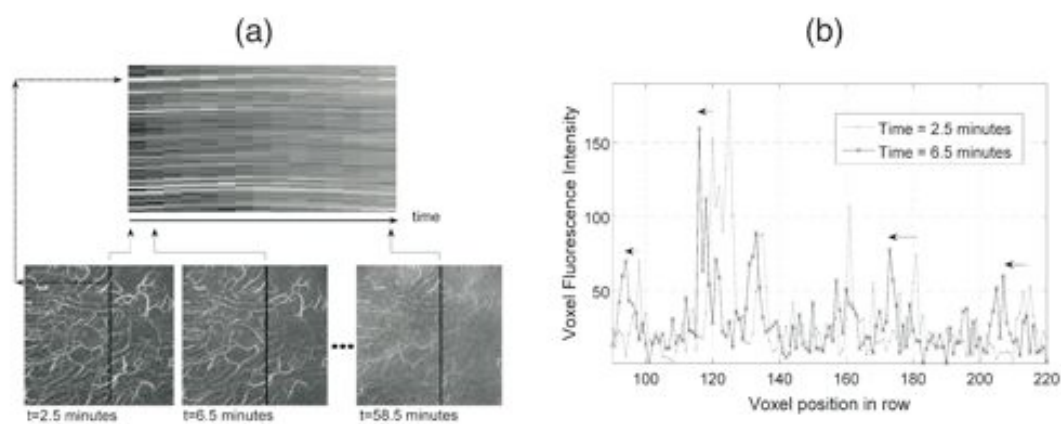


Figure 2. (a) A time-cut (top image) to illustrate the tissue movement with time of one data set. Single columns (one voxel of width and depth) of data are extracted from 2-D

images at each time point and placed next to each other to form a new image, having the time as the horizontal axis. Three 2-D images from the whole time series are shown to illustrate the procedure. Dashed arrows indicate bright intra-vascular tissue in the first 2-D image and its corresponding voxel in the first column. Solid vertical lines indicate the exact cut from where data for the columns are obtained and the solid arrows indicate the position on the column at which they are placed. The movement is manifest as the variation of the intensity upwards and then downwards with time. (b) Two 1-D lines corresponding to the intensity of the voxels of one of the columns selected above at two different time points ($t = 2.5, 6.5$ minutes). Notice the shift of the peaks to the left.

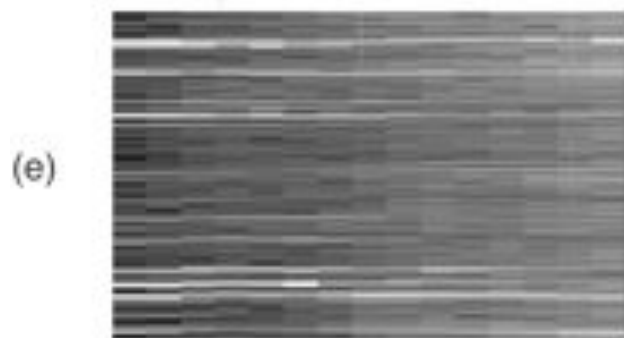
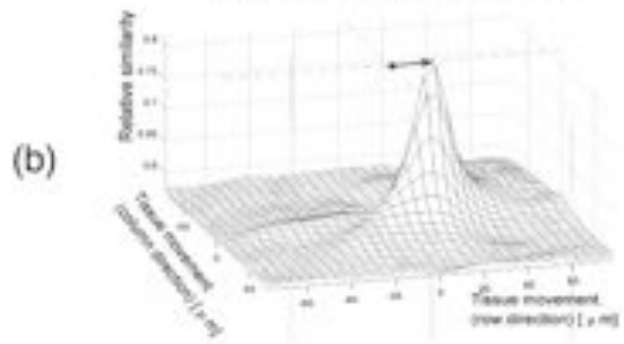
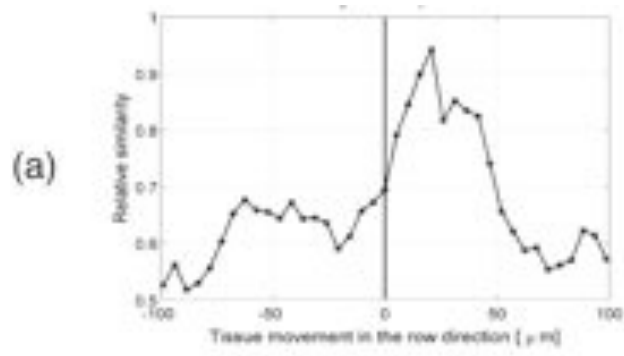


Figure 3. Registration of data through cross correlation. (a) The cross correlation of the two 1-D signals shown in figure 2 (b). The degree of movement of the signals is depicted by the maximum value of the relative similarity (close to 95%) being to the right of the central value. (b) Cross correlation of two 2-D signals displayed as a 3-D mesh. Notice again how the maximum is shifted from the centre. The movement in the direction of the rows is close to 20 μm , while there is no apparent movement in the direction of the columns. The arrow indicates the movement of the tissue. Rigid and non-rigid registration maps (c, d) denoting the direction of the displacement required to correct for the movement of the 15 partitioned regions of the data. (e) Registered time cut. The curved lines that revealed the temporal movement of the images in figure 2 (a) appear as straight lines in the registered set.

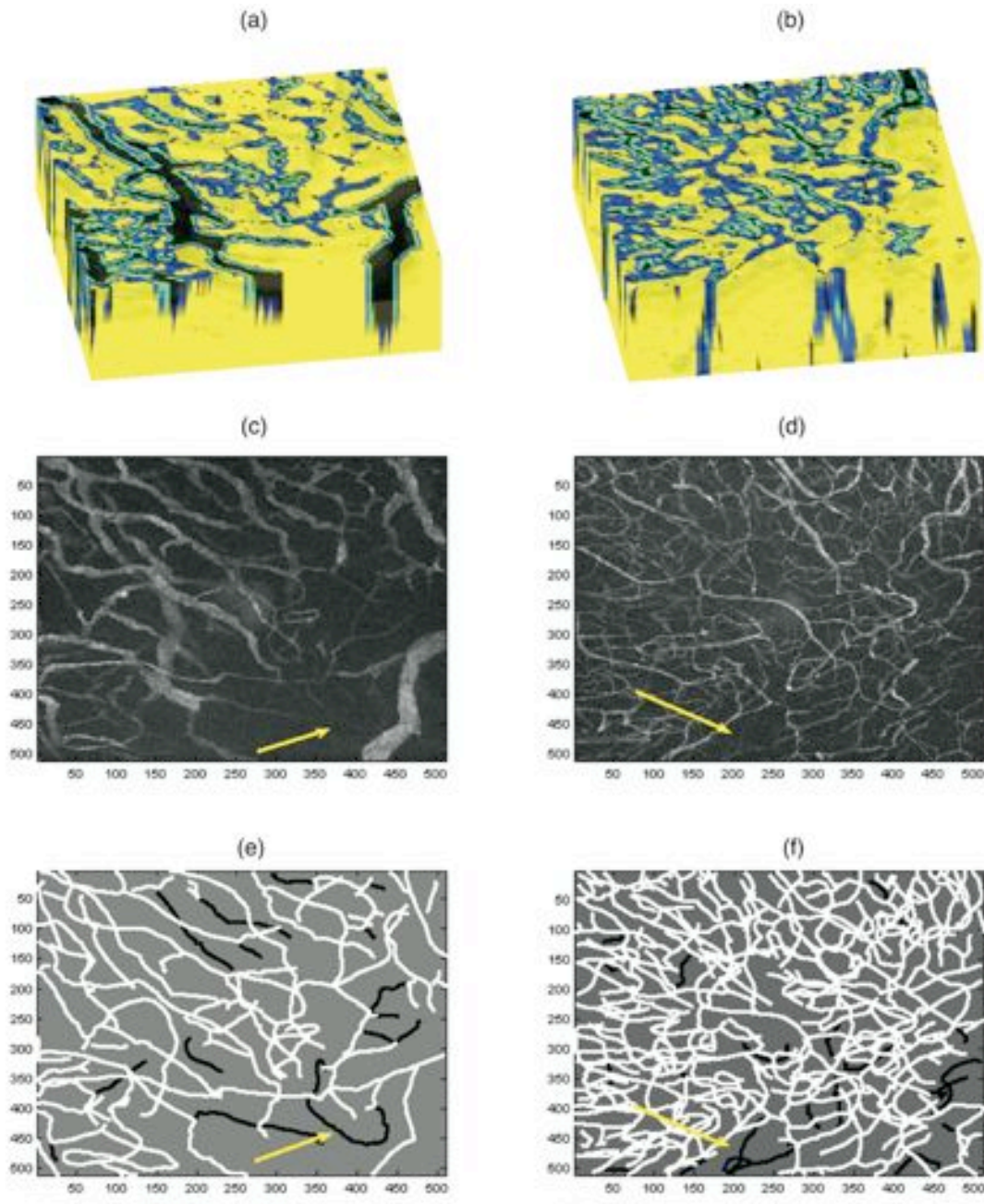


Figure 4. Comparison of the image segmentation algorithm with a manual method. (a, b) 3-D rendering of the class masks for two tumours. Intra-vascular voxels are labelled in black, extra-vascular voxels in yellow and boundary region in blue, with a lighter shade for the voxels closest to the intra-vascular region. In these two tumours there were insignificant numbers of unclassified voxels. The rendering was performed with transparency and details of different slices can be seen. (c, d) Maximum intensity projection of the intensities of two data sets. The arrows point to regions of intra-vascular

tissue with low intensities. (e, f) Comparison with manually segmented vessels. The vessels that were correctly segmented with the algorithm (those with more than 50% points correctly classified, see text) are labelled in white and those that were not are labelled in black. The arrows show two regions of low intensity where the segmentation with the proposed methodology detects less than 50% of the points of the manually segmented traces.

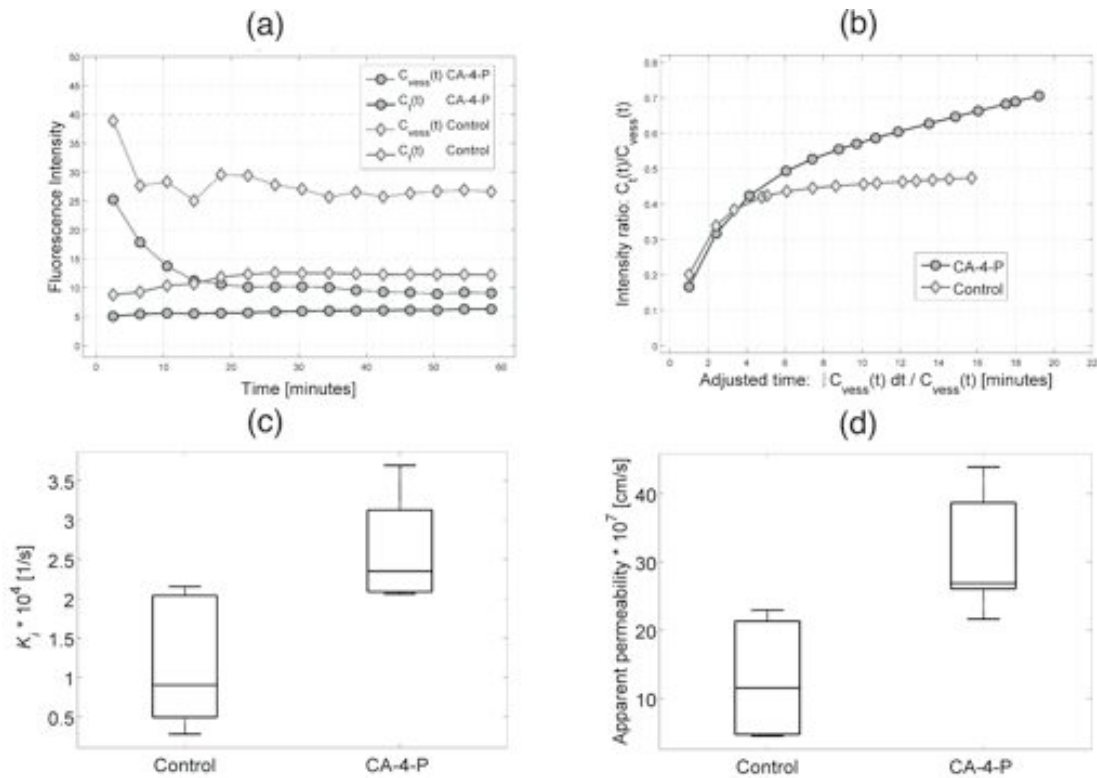


Figure 5. (a) Time-activity curves of the intensities of intra-vascular tissue ($C_{vess}(t)$) and extra-vascular tissue ($C_t(t)$) versus time for two data sets, one control and one treated with CA-4-P. While C_{vess} decreased exponentially, C_t increased steadily. It was assumed that this increase is due to the extravasation of the marker. The vertical axis denotes average intensity in the intra- and extra-vascular regions and the horizontal axis denotes time after fluorophore injection. (b) Transformed time plots for the same control and CA-4-P-treated tumours. Data from time-activity curves were transformed, as described by Patlak et al [21] (see text for details). The vertical axis denotes the ratio of intensities in the intra- and extra-vascular regions and the horizontal axis denotes an adjusted time,

such that the curves represent the intensity ratio versus time curves that would have pertained in each case had the input functions (C_{vess} versus time) been constant throughout the time-course of the experiment. The slope of the linear section of the plot provides the estimate of K_i . Notice that the treated case has a higher slope than the control. (c) Box plot (lines at the lower quartile, median, and upper quartile values) of the K_i product for the two groups ($1.13 \pm 0.33 \times 10^{-4} \text{ sec}^{-1}$ for the controls and $2.59 \pm 0.20 \times 10^{-4} \text{ sec}^{-1}$ for CA-4-P, $p = 0.0014$) and (d) Box plot of the apparent permeability P for the two groups ($12.76 \pm 3.36 \times 10^{-7} \text{ cm/s}$ for controls and $30.94 \pm 2.64 \times 10^{-7} \text{ cm/s}$ for CA-4-P, $p = 0.0009$). Both box plots denote statistical difference between treated and control groups.